Palaeopermeability anisotropy and geometrical properties of sealed-microfractures from micro-CT analyses: An open-source implementation

Rodrigo Gomila[a,b,*], Gloria Arancibia[a,b,c], Domingo Mery[b,d], Mathias Nehler[e], Rolf Bracke[e], Diego Morata[b,f]

[a] Departamento de Ingeniería Estructural y Geotécnica, Pontificia Universidad Católica de Chile, Av. Vicuña Mackenna 4860, Macul, 7820436, Santiago, Chile
[b] Andean Geothermal Center of Excellence (CEGA, FONDAP-CONICYT), Universidad de Chile, Santiago, Chile
[c] Centro de Investigación en Nanotecnología y Materiales Avanzados (CIEN-UC), Pontificia Universidad Católica de Chile, Santiago, Chile
[d] Departamento de Ciencias de la Computación, Pontificia Universidad Católica de Chile, Santiago, Chile
[e] International Geothermal Centre (GZB), Bochum, Germany
[f] Departamento de Geología, Universidad de Chile, Santiago, Chile

ABSTRACT

Fault zone permeability and the real 3D-spatial distribution of the fault-related fracture networks are critical in the assessment of fault zones behavior for fluids. The study of the real 3D-spatial distribution of the micro-fracture network, using X-ray micro-computed tomography, is a crucial factor to unravel the real structural permeability conditions of a fault-zone. Despite the availability of several commercial software for rock properties estimation from X-ray micro-computed tomography scanning, their high cost and lack of programmability encourage the use of open-source data treatment.

This work presents the implementation of a methodology flow for the quantification of both structural and geometrical parameters (fractures density, fractures aperture, fractures porosity, and fractures surface area), and the modeling of palaeopermeability of fault-related fractured samples, with focus in the proper spatial orientation of both the sample and the results. This is performed with an easy to follow step-by-step implementation, by a combination of open-source software, newly implemented codes, and numerical methods. This approach keeps track of the sample's spatial orientation from the physical to the virtual world, thus assessing any fault-related palaeopermeability anisotropy.

1. Introduction

Fault zones and their related fracture networks are a key factor in controlling the migration of geofluids through the Earth's crust (Caine et al., 1996; Sibson, 1996; Cox et al., 2001; Faulkner and Rutter, 2001; Uehara and Shimamoto, 2007; Boutareaud et al., 2008), and therefore the understanding of the spatial distribution of their hydraulic properties (i.e., porosity [Φ] and permeability [k]) is crucial in the assessment of fault zones behavior for fluids.

Fault zones involves strain, distributed in its fault core and damage zone. The fault core localizes most of the strain, whereas the damage zone is a relatively low strain zone that surrounds the fault core. In low porosity rocks, the damage zone generally consists of second-order structures such as veins, fractures and subsidiary faults (Wibberley and Shimamoto, 2003; Mittempergher et al., 2009; Faulkner et al., 2010). Thus, fault damage zones are recognized to play an essential role as

high porosity and permeability conduits for hydrothermal fluids due to its enhanced fracturing at micro and macro scales (Caine et al., 1996; Kim and Sanderson, 2004; Morton et al., 2012; Arancibia et al., 2014).

The accurate and quantitative estimation of the fracture network properties in fault damage zones rely in their important role in several geological processes such as, seismic hazard (Evans et al., 1999; Li et al., 2007), hydrocarbon migration (Aydin, 2000; Boles et al., 2004), fluid permeability (Bellot, 2008; Roques et al., 2014; Gomila et al., 2016), geothermal exploration (Rowland and Sibson, 2004; Brogi, 2008; Watanabe et al., 2017), hydric resources (Berkowitz, 2002; Bense et al., 2013) and mineral resources (Craw and Campbell, 2004; Tripp and Vearncombe, 2004).

Hydraulic properties of fractured rocks and fault zones have been classically estimated by laboratory measurements (Morrow and Lockner, 1994; Mizoguchi et al., 2008; Ran et al., 2014; Christensen and Tanino, 2017), from the back analysis of hydraulic tests in boreholes

---

(Hung et al., 2009; Lockner et al., 2009; Ran et al., 2014), and lately by numerical analyses of fluid injection in fault zones (Jeanne et al., 2013). However, these estimations are not based in hydrothermally filled fractures, which reflects the instantaneous flux of fluids and record the palaeopermeability condition of the fault-fracture system at seismogenic depth (Gomila et al., 2016).

Intrinsic permeability (k), is defined as the physical property - the ability - of a porous material (i.e., a rock) to transmit a single-phase fluid (Latief et al., 2014), appears in Darcy's law (Eq. 1) as follows:

$$\frac{Q}{A} = -\frac{k}{\mu}\frac{\Delta P}{L} \qquad (1)$$

where Q is the global flow rate through the porous medium (m^3/s), and A is the cross-section of the sample which the fluid goes through (in m^2). k is the absolute permeability (m^2); μ is the dynamic viscosity of the flowing fluid (in Pa $\times$ s); ΔP is the pressure gradient applied around the sample (in Pa), and L is the length of the sample in the flow direction (m).

Lately, permeability has been calculated using Lattice-Boltzmann Methods (LBM) (Keehm et al., 2004; Okabe and Blunt, 2004; Grader et al., 2009; Degruyter et al., 2010; Sun et al., 2011; Latief et al., 2014; Anissofira and Latief, 2015; Perumal and Dass, 2015; Bultreys et al., 2016), a largely used and validated Computational Fluid Dynamics (CFD) numerical method for simulating viscous fluid flow (Wildenschild and Sheppard, 2013; Vlahinić et al., 2014; Voorn et al., 2015; Ju et al., 2017). The LBM approximates the continuous Boltzmann equation by discretizing the physical space into a set of uniformly spaced nodes (lattice), where packets of moving and interacting particles are introduced, thus defining a particle distribution for each possible particle velocity vector at each node of the lattice (Sukop and Thorne, 2006; Bultreys et al., 2016).

Intrinsic permeability (k; in m^2) can be calculated using the open-source LBM solver called Palabos (Parallel Lattice Boltzmann Solver, www.palabos.org). The methodology used by Palabos, to calculate the absolute permeability of the rock, involves solving a modified version of Darcy's equation (Eq. 2). Q/A is denoted as $\langle v \rangle$ and accounts for the superficial or mean fluid flow velocity through the porous medium or Darcy's velocity, and where the discretized space is, for propose of this study, obtained from X-ray micro-computed tomography (μ-CT) (Fig. 1).

$$k = \frac{\mu \langle v \rangle}{dP/dL} \qquad (2)$$

μ-CT provides 3D structural information of rocks based on the attenuation of X-rays when they travel through the sample (Ketcham and Carlson, 2001; Baker et al., 2012; Cnudde and Boone, 2013; Wildenschild and Sheppard, 2013; Bultreys et al., 2016). The obtained images are digitally reconstructed into a 3D-volume, denoted in gray-scale, representing the spatial distribution of the linear attenuation coefficient. This 3D-volume is then segmented as binary images where the discretized space for modeling is isolated.

It is often worthwhile to use these segmented discretized spaces in the generation of 3D pore networks, for later characterization of the geometrical and hydraulic properties of the samples (Wildenschild and Sheppard, 2013; Guibert et al., 2015; Voorn et al., 2015; Jarzyna et al., 2016). However, up to which point the characterized geometrical and hydraulic properties, extracted from the 3D discretized spaces, are representative of a flow model (as in Davy et al., 2006) is still openly debated. Fractures have been studied with μ-CT from different perspectives. Hirono et al. (2009) estimated the dilative shear porosity developed during the 1999 Taiwan Chi-Chi Earthquake in core samples within the Chelungpu Fault. Karpyn et al. (2007) studied the effects of fracture morphology on the distribution and transport of immiscible fluid phases through a fracture, and Anissofira and Latief (2015) estimated both granular and crack-type permeability for a geothermal reservoir rock.

Despite the availability of several commercial software for rock properties estimation from μ-CT scanning, their high cost and lack of programmability (due to a close-code policy) encourage the use of open-source data treatment. Recently, some open-source software packages have been released aimed at the segmentation of fractures (Voorn et al., 2013; Deng et al., 2016). However, the main issue is that they are limited by the presence of a heterogeneous material being cut by fractures, as in the case of this study, making them unfit to use.

The purpose of this work is to present a workflow implementation as a methodology, with the use of open-source software (ITK-SNAP©, ImageJ©, and Palabos©), and newly implemented Matlab© scripts, for the geometrical and the spatially-dependent hydraulic properties analyses of hydrothermally-sealed microfracture network of a fault damage zone, in spatially-oriented 3D-volumes.

2. Proposed methodology implementation

For the proper estimation of the geometric and hydraulic properties of sealed microfracture network from μ-CT images, we used a fault damage zone sample studied by Gomila et al. (2016). The used microfractured sample corresponds to a hypidiomorphic equigranular gabbro located at 50 m east of the Jorgillo Fault, an exposed 20 km long, left-lateral strike-slip fault, which juxtaposes Jurassic gabbro against metadiorite belonging to the Atacama Fault System in northern Chile.

The gabbro, at the macroscopic scale, shows a steeply dipping, subparallel to the main fault strike, magmatic layering of plagioclase and pyroxene, ranging from a few centimeters to tens of centimeters in thickness. Whereas, at the microscopic scale, the rock shows a grain size ranging ca. 0.5–3.0 mm. Its major mineralogical components (Fig. 2)
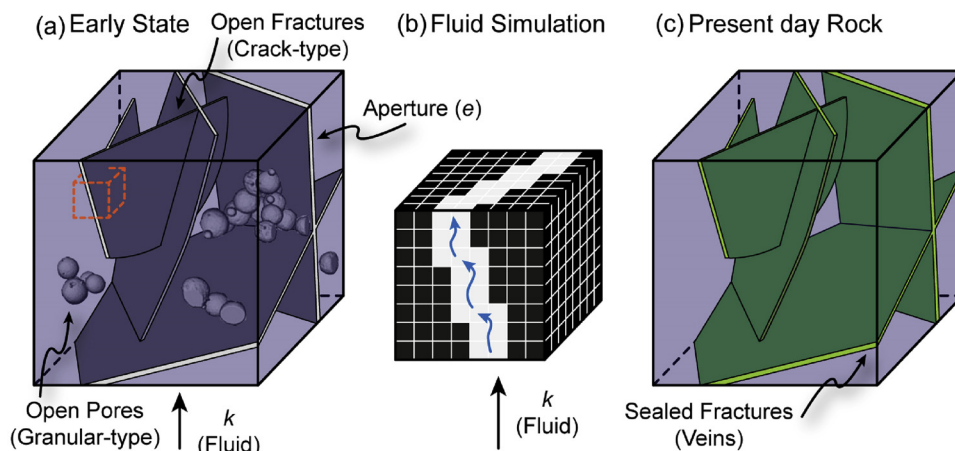

Fig. 1. The aim of this work. At an early stage (a) fractures are created, either in a porous or non-porous media, thus allowing the transmission of fluids through the rock volume. b) Permeability is modeled using LBM through a discretized space (i.e., small red box in a). c) The evidence of fluid-flow through fractures are now seeing as sealed fractures in the rock (For interpretation of the references to colour in this figure legend, the reader is referred to the web version of this article).
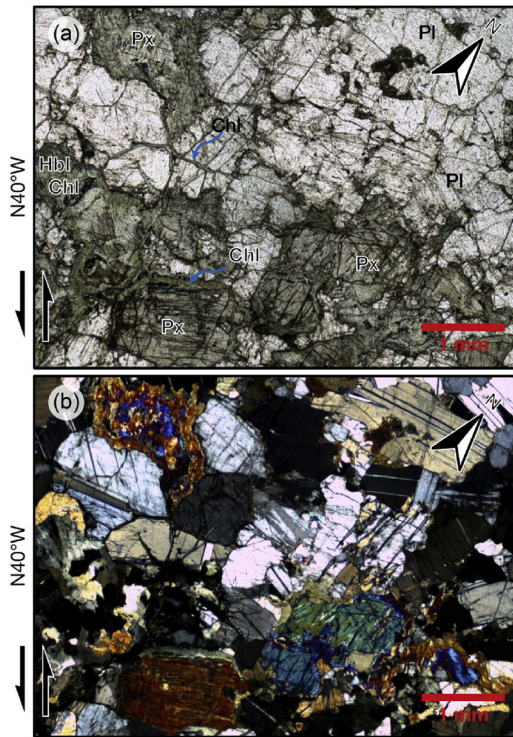
Fig. 2. Microscopic characterization of the studied sample. (a) Plane-polarized light photomicrograph. Note the chlorite (Chl) sealed microfractures. (b) Cross-nicols light photomicrograph.

are ca. 60% subhedral plagioclase (Pl) and ca. 40% subhedral pyroxene (Px). Plagioclase shows undulose extinction whereas the pyroxene presents reaction rims of hornblende (Hbl) which are partially or entirely replaced by chlorite (Chl). Sealed-microfractures are composed only of chlorite and show no evidence of shear (Fig. 2).

We propose a methodology based on a four-step implementation (Fig. 3): 1) Pre-Scanning stage, which consists in the preparation of the sample before scanning, where the correct field-sample acquisition and laboratory-preparation of the oriented hand-sized sample are crucial for the correct assessment of the spatial-dependent hydraulic properties. 2) Digital Image Acquisition stage, where the rock is scanned and further reconstructed, and a sub-volume is obtained and properly prepared for the latter 3) Image Processing stage, in which the segmentation of the microfracture matrix is obtained and filtered. Finally, we propose a 4) Post-Processing stage, in which the geometrical (fracture specific surface area, fracture aperture, fracture density, and fracture porosity), and hydraulic properties (palaeopermeability) are calculated.

2.1. Sample acquisition for proper oriented μ-CT scanning

Sample orientation is a key factor in assessing any possible spatial anisotropy in the hydraulic properties of a rock, and therefore, a fault zone. Remarkable examples of spatially oriented samples and results are shown by Tarquis et al. (2008) and De Boever et al. (2015). However, it is not possible to follow the entire orientation process from the field to the modeling results. In this work, after the field collection of spatially oriented hand-sized samples, an orthogonal to the average direction of the medium stress axis (σ_2) plate should be prepared. In the case of the selected sample (from a vertical strike-slip fault), horizontally oriented plates were prepared (Fig. 4a and b). Later, a parallel to the average direction of the medium stress axis (σ_2) plug should be drilled, thus obtaining vertically oriented plugs. The plugs were drilled
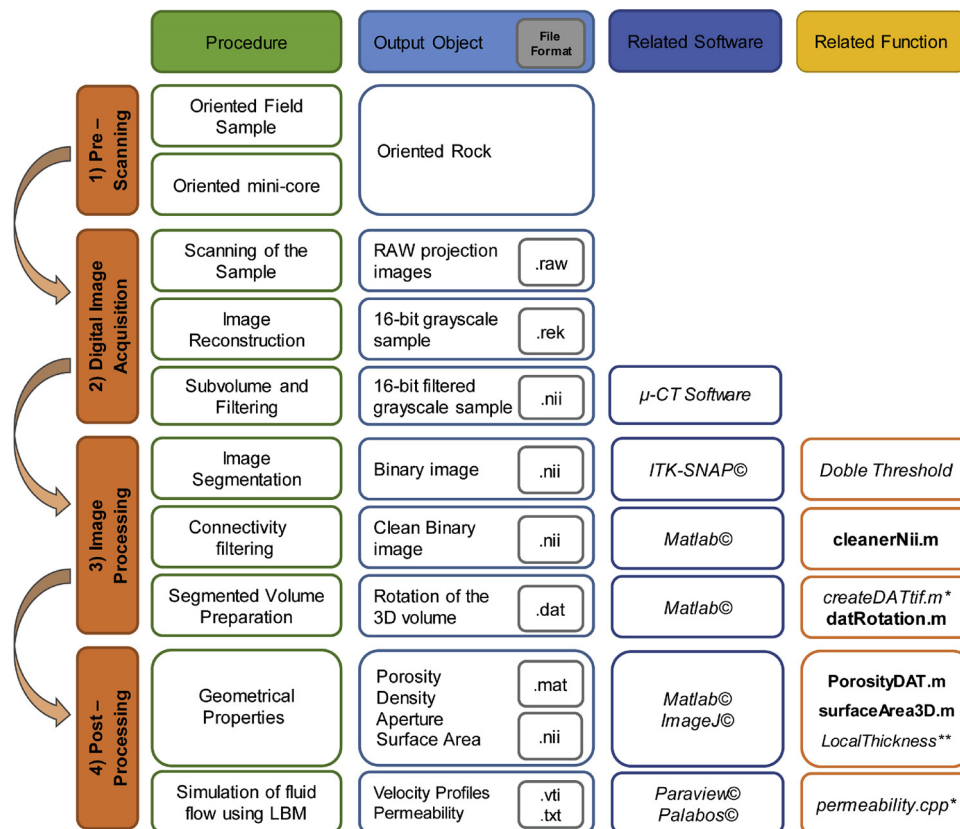

Fig. 3. Methodology Flow for proper analysis and related functions (implemented in Matlab©) or used software. * denotes a modified script from Degruyter et al. (2010), ** denotes function from Dougherty and Kunzelmann (2007). Functions in bold letters denote functions developed in this work. N/A = not applicable.
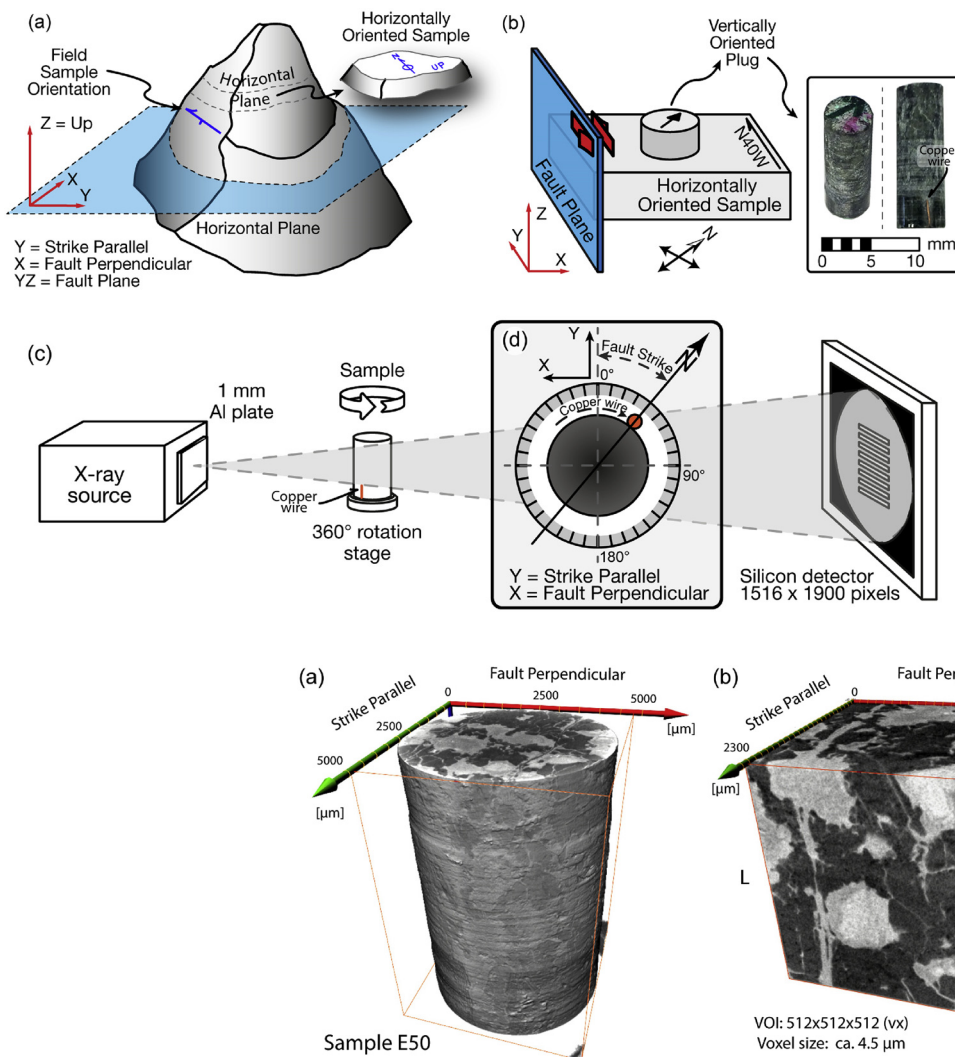
Fig. 4. Sample preparation and oriented μ-CT scanning. a) Schematic representation of the field sample orientation and the horizontally oriented plate. b) Schematic representation of the horizontally oriented plate and the position of the oriented plug. Inset showing vertically-oriented plug, showing North direction represented by the green arrow, and the North-Down direction represented by copper wire. c) Schematic diagram of the plug scanning. Main parts of the set-up is pointed out. d) Set-up of the vertically oriented plug (looking down view) (For interpretation of the references to colour in this figure legend, the reader is referred to the web version of this article).
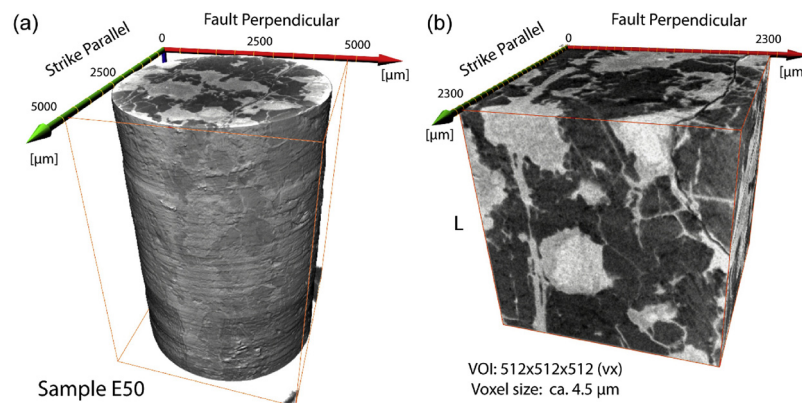

Fig. 5. Acquired digital images. a) Reconstructed (16-bit grayscale) oriented volume of the entire oriented plug. b) Volume of Interest (VOI) obtained as a sub-volume within the oriented plug.

with a diamond mini core drill of 5 mm in diameter and, a thread of a higher density material than the plug (i.e., a thin copper wire) was attached at the bottom side of the sample representing the north-down orientation (Fig. 4b), thus preserving the plug's orientation into the digital world after scanning (Fig. 4c and d).

2.2. Digital image acquisition from X-ray micro-computer tomography

μ-CT provides 3D structural information of rocks based on the attenuation of X-rays when they travel through the sample. This attenuation depends on the X-ray energy, the atomic electron number, and bulk density of the sample, and quantified by the Lambert–Beer law. The obtained images are digitally reconstructed into a 3D-volume, denoted in voxels with 2^{16} gray-values, representing the spatial distribution of the linear attenuation coefficient (Mutina and Koroteev, 2012).

2.2.1. Data acquisition and reconstruction

To represent the internal 3D microfracture structure of the sample, we scanned the microfractures with a μ-CT scanner at the International Geothermal Centre (GZB) in Bochum, Germany. X-rays were generated in a transmission target X-ray tube with an acceleration voltage of 80 kV and target current of 25 μA. The focal spot size on the diamond/tungsten target was about 5 μm. The X-ray beam was filtered using a

1 mm aluminum plate before passing the sample to minimize beam-hardening artifacts (Brooks and Di Chiro, 1976). The reconstruction process is based on a Radon transform in the form of a convolution and back filter (Feldkamp et al., 1984) and performed with the Volex reconstruction engine (Fraunhofer-Allianz Vision, 2012). 1520 images were taken during a full rotation of the sample during the scanning process, resulting in a voxel resolution (or grid spacing: d) of ca. 4.5 μm.

We positioned the core-plug on the rotation stage in such a way that we preserved its orientation related to the fault in the reconstructed gray-value images (Fig. 4e). The positioning is performed by placing the plug at a specific angle with respect to the orthogonal between the X-ray source-detector line (Fig. 4f). This angle corresponds to the fault strike, and so, the faces of the resulting reconstructed voxels are properly oriented into the fault coordinates system (X: fault-perpendicular; Y: strike-parallel; Z: vertical).

2.2.2. Sub-volume selection

After data reconstruction (Fig. 5a), a volume of interest (VOI), for a reasonable porosity and permeability estimation, must be chosen. We define a characteristic length scale (ξ) equivalent to the mean hydraulic radius, which in the case of fractures corresponds to half the mean aperture (Walsh and Brace, 1984; Berg, 2014) obtained, in an early stage, from thin sections measurements. Keehm and Mukerji (2004) demonstrate that permeability is reasonably determined when the size
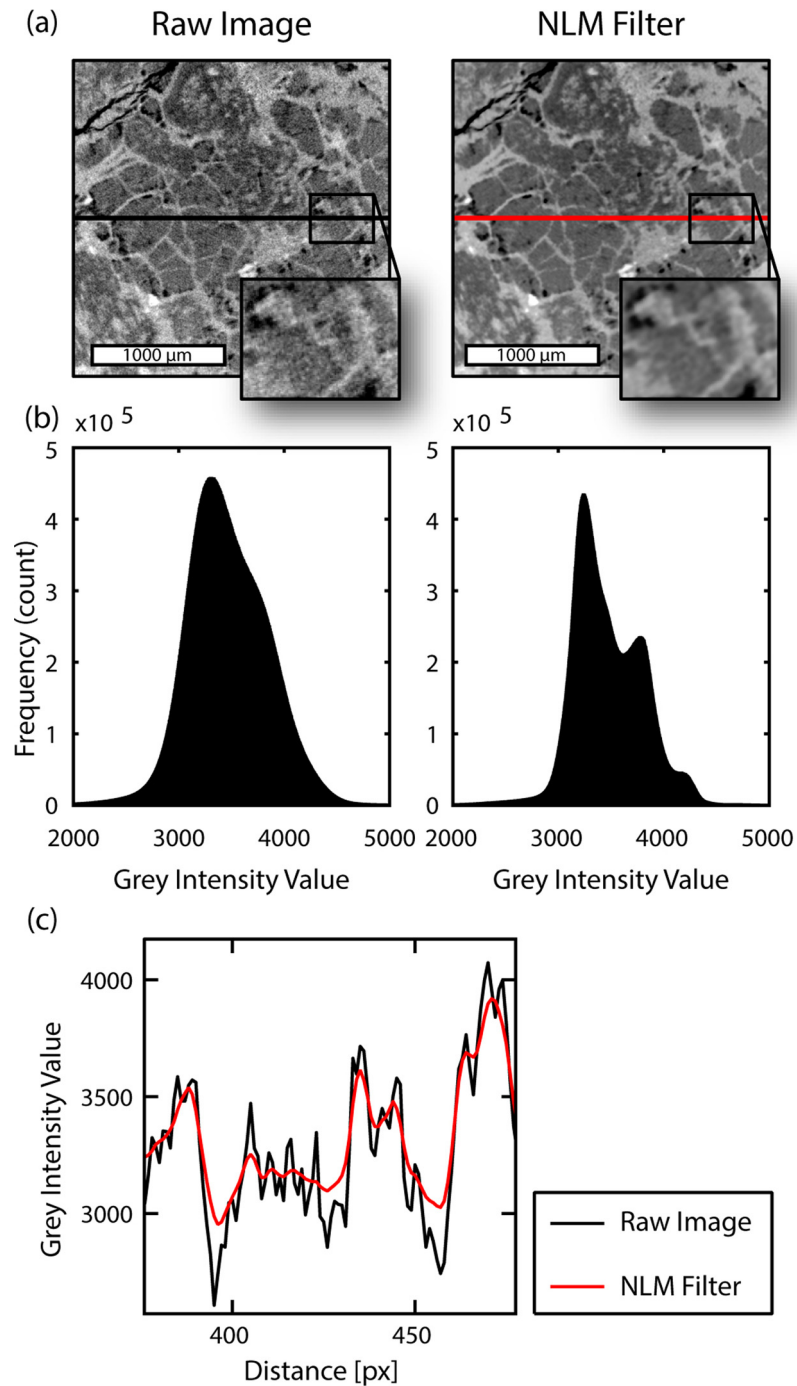
Fig. 6. Effect of the filtering process in the 3D volume and its corresponding intensity histogram. a) Sections of a 3D volume as seen in the RAW image and the Non-Local Means filter with detailed inset for visual comparison of the results. b) Frequency histograms (following the same order than the upper row) showing how the applied filter improve the sharpness in phase boundaries. c) Comparison between gray intensity values located across the insets in (a).

of the digital rock (*L*) is greater than 10 times the half mean aperture (*L* ≥ 10ξ) and grid spacing (resolution) is lower than a 10th of the half mean aperture (*d* ≤ *ξ/10*). Although their approach focused on extracting hydraulic properties from homogeneous porous media (the Berea Sandstone), it is a good proxy for early estimation of a reasonable big sub-sample size.

We used a fault damage-zone sample studied by Gomila et al. (2016), who measured the 2D mean apertures in thin section (ranging ca. 20–100 μm). Considering this range in apertures, and the fact we are physically limited by the size of the sample, we chose a VOI of 512^3 voxels. The size of the digital rock (*L*) is ca. 2300 μm in the axes direction (Fig. 5b), so it would be as representative as possible of the

fracture porosity, fracture density, and permeability of the sealed microfracture network.

Davy et al. (2006) suggested two types of flow structures, namely channeled and distributed, could act independently of the length scale of the hydraulic model (either the connection, channeling or homogenization scales). To assess both types of flow structures, and up to which point the distribution of fractures within the VOI is homogeneous or heterogeneous, we deliberately avoided a major microfracture. This major feature was marked both in the scanned sample and the segmented image. To remove the major microfracture, we chose sub-volumes of the same sample, where the major microfracture was absent. Nevertheless, the relationship between the size of the digital rock and
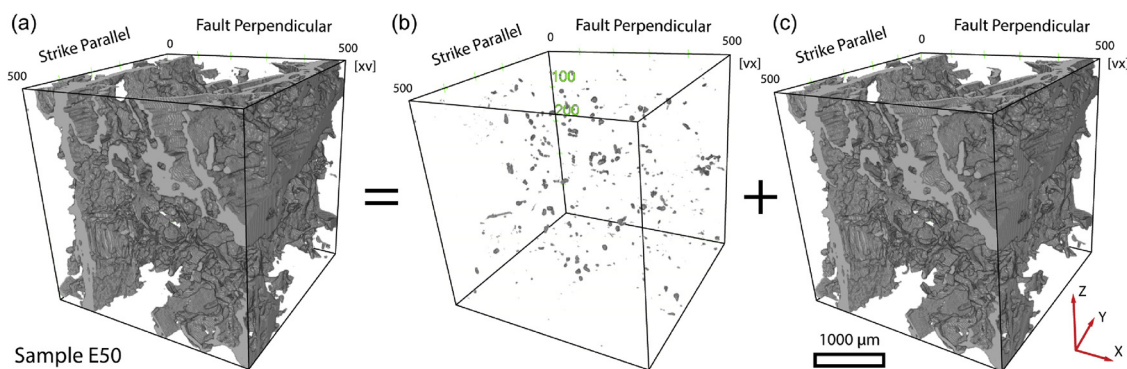
Fig. 7. Segmented chlorite-sealed microfracture network. a) 3D volume segmentation before cleansing. b) 3D volume of the isolated unwanted small and unconnected volumes. c) Cleansed segmentation 3D volume.

the mean hydraulic radius ($L \geq 10\xi$), was maintained.

2.3. Image processing

2.3.1. Image filtering

When noise is present in an image, the proper detection of boundaries between phases can be difficult (Vlahinić et al., 2014). Subsequently, to remove the image noise while maintaining sharp edges between phases an image filter must be applied to the entire data-set. Several filtering algorithms have been defined over the years. However, all the de-noising approaches use some kind of average, where the most applied are the Medium, Gaussian and the Non-Local Means filters (Vlahinić et al., 2014).

Gaussian and Median filters are some of the most classically applied filters algorithms (Buades et al., 2008; Andrä et al., 2013; Zhang et al., 2013; Vlahinić et al., 2014). Both use lowpass filters to reduce the contrast and soften the edges of objects in an image. However, although they reduce contrast, they tend also to defocus the image.

The de-noise algorithm applied in this work is the Non-Local Means (NLM) filter (Buades et al., 2008). This filter has shown to be an extremely accepted method for noise-reduction in μ-CT images (Andrä et al., 2013; Zhang et al., 2013; Vlahinić et al., 2014), as it can reduce noise within phases while preserving sharpness at grain boundaries (Vlahinić et al., 2014). The filtering process uses a search window in which compares the neighborhoods of all voxels in the given search window. The similarity between the neighbors determines the weight with which the value of a voxel in the search window will influence the new value of the current voxel. The final weights are determined by applying a Gauss kernel to the similarity values. The NLM has the advantage of improving phase boundaries (Fig. 6), thus allowing better processing of the image.

2.3.2. Image segmentation

The segmentation process consists of the isolation and identification of discrete mineral phases in an image (Wildenschild and Sheppard, 2013), distinguishable by different gray intensity values, and the further binarization of the 3D-volume. Segmentation of the chlorite-sealed microfractures network was performed by the user-guided open source ITK-SNAP® software (Yushkevich et al., 2006), an application classically used to segment 3D structures in medical images. In simple words, the software uses an active contour segmentation method in which several seeds are implanted inside the desired feature where a double threshold (in gray-scale) is imposed. Then, the seeds expand in every direction through the 3D image until the thresholds are reached. Whenever there is a similarity between the attenuation coefficient (grey scale) of the sealed-microfracture and its surrounding fractured mineral (in this case chlorite-altered pyroxene), it is necessary to make the segmentation process manually.

2.3.3. Connectivity filtering

Once the chlorite-sealed microfracture network is isolated (Fig. 7a), and to eliminate any unwanted volume resulted as artifacts produced during the segmentation, and that does not represent part of the microfractures, a two-steps filtering of the segmented volume is performed (with the script **cleanerNii.m**). First, (1) by removing 6 voxels per side of the entire segmented volume (hence reducing the size of the volume by 12 voxels each direction) any possible segmentation-related edge issue of the volume is eliminated, and second, (2) by eliminating any small isolated volume (Fig. 7b) under the desired threshold (in this case < 1000 voxels). By carrying out this procedure, it is possible to obtain a simplified dataset without isolated voxels, not relevant for flow simulations (Fig. 7c), but that would eventually, increase the desired fracture porosity value, where further geometrical and hydraulic analyses will be performed. Afterward, sequential 2D slices in the Z direction are produced.

2.3.4. 3D-volume preparation for geometrical and hydraulic analyses

With the use of a modified script (createDATtif.m), a new 3D-volume is created. This procedure has been previously presented by Degruyter et al. (2010), and consists in assigning a specific value to each voxel in the selected VOI: 0 for a fluid voxel (related to the sealed microfractures), 1 for a voxel that is in contact with the pore voxel (thus establishing the boundary conditions), and 2 for no-dynamic background voxels (related to the non-fractured rock).

Permeability simulations are always performed in the same direction, like measurements on a permeameter in the non-virtual world. So, to be able to run permeability simulations through every direction of the VOI, this should be rotated related to its axes. This rotation is performed with the script **datRotation.m**, thus creating two new volumes, one with the fault-perpendicular axis (X) in the direction of the fluid simulation, and other with the strike-parallel axis (Y) in such condition.

2.4. Post-processing

2.4.1. Geometrical properties measurement

Fractures aperture (*e*) were extracted before μ-CT scanning from thin section analysis presented by Gomila et al. (2016). Such approximations, however, might entail measurement problems due to user sampling bias, the constrict amount of aperture measurements, probably lack statistical representability of the microfracture network, and more important is the use of 2D sections to represent a 3D geometry. To overcome this issue, we will work with the segmented 3D-volumes instead. Dougherty and Kunzelmann (2007), proposed a plugin implemented for the public domain software ImageJ (Schneider et al., 2012), called Local Thickness which is used to determine the aperture distribution of the full sample (Fig. 8a). This approach uses the larger possible spheres fitted within the segmented fractures, which relies on
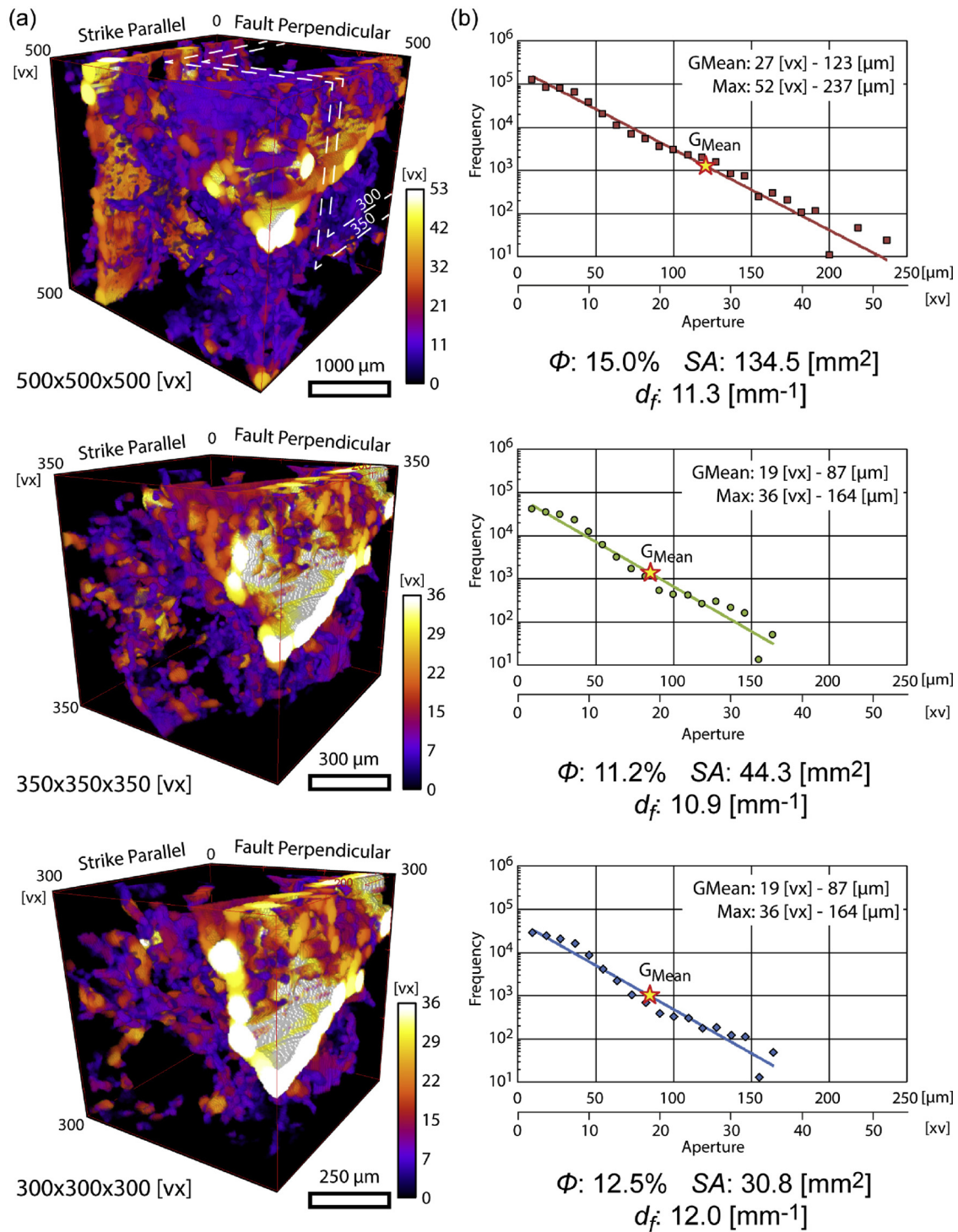
Fig. 8. a) 3D-volumes of different sizes (500³, 350³,300³ voxels) showing the aperture distribution of the sealed microfracture network. b) Aperture distribution for the entire 3D-volumes for each dataset (on the left). Geometrical mean (G_Mean), maximum aperture (Max), fracture porosity (Φ), fracture surface area (SA), and fracture density (d_f) are shown.

the fact that, for fractures, the aperture can be represented as the diameter of a fitted sphere. The full aperture distributions (Fig. 8b) represents the amounts of voxels at each bin divided by the volume of each sphere size in the same class, thus compensating for volume bias (Voorn et al., 2015).

Fracture porosity (Φ) is assumed to be represented by the entirely connected fracture network. Therefore, Φ is measured as the ratio between open voxels (represented by zeros in the segmented volume) and the total number of voxels in the REV. This procedure is done with the script **PorosityDAT.m**, and the result is given as a percentage.

Fracture surface (SA) corresponds to the fracture-matrix boundary area. It is calculated directly from the 3D-volume, by doing a convolution to count the exposed faces, then labeling and counting the pixel values. Then, the values are recursively obtained for every isolated region in the volume and added to get the microfracture network total surface area, performed by a modified script (**surfaceArea3D.m**). Finally, to convert the obtained value to real units [mm²], the µ-CT spatial resolution is used.
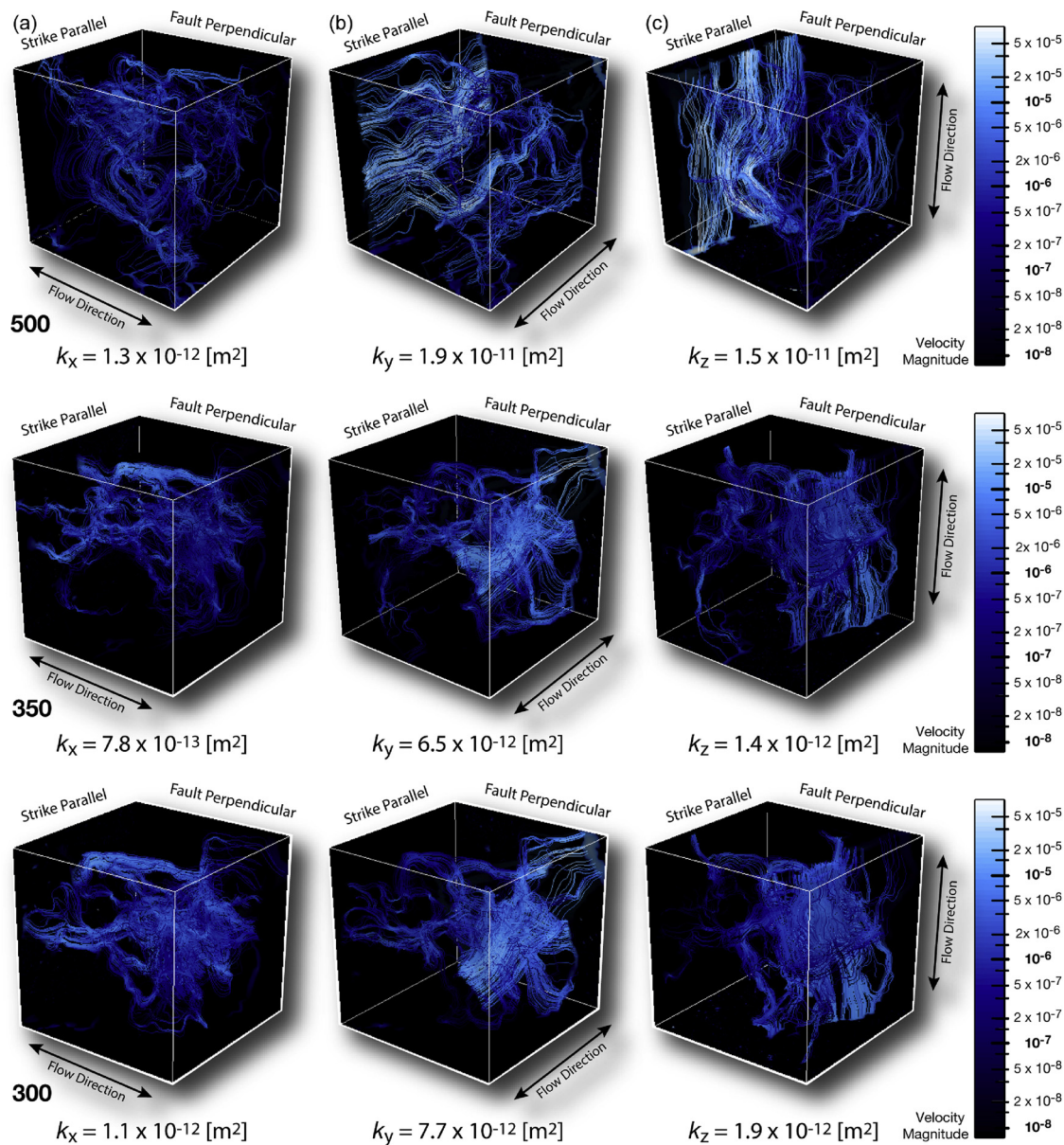
Fig. 9. Velocity profiles and modeled permeability values in the different axes for each 3D-volumes (500^3, 350^3, and 300^3 voxels). Fault perpendicular (k_x), strike parallel (k_y), and vertical (k_z). Main velocity scale in log scale.

Fracture density (d_f) [mm^{-1}], is expressed as the ratio between the fracture-matrix boundary area (namely fracture surface in mm^2) and the total sample volume [mm^3] (Singhal and Gupta, 2010). This property has also been named as specific surface area (Mostaghimi et al., 2013; Bazaikin et al., 2017) or fracture intensity (Karcz and Dickman, 1979).

2.4.2. Fluid-flow simulations

Permeability was calculated using the LBM, where a modified C++ script presented by Degruyter et al. (2010) was used. The rotation of the VOI in relation to their axes allows the modeling of the palaeopermeability for the three axes, thus obtaining permeability values referred to the main fault principal axes (Fig. 9).

The results of the simulation are a. vti file, where the velocity distribution is written, and a. txt file, where the permeability results are listed in lattice units. The modeled permeability is the lattice permeability times the squared μ-CT spatial resolution (Degruyter et al., 2010). The. vti file can be read in ParaView (Ahrens et al., 2005; Ayachit, 2015), an open-source, multi-platform data analysis and

visualization application, where the velocity fields can be visualized (Fig. 9).

3. Results and discussion

3.1. Geometric and hydraulic properties distribution

While the differences in fracture density, for the different volumes, is at most 1.1 mm^{-1} (between 10.9 mm^{-1} and 12.0 mm^{-1}; Fig. 10a), porosity values vary from 15.0% to 11.2% (Fig. 10b). These small changes in both fracture density and fracture porosity points towards the selected volume for three sub-sample sizes are somehow representative of these geometrical properties. The obtained fracture density values are consistent with microfracture density shown by Mitchell and Faulkner (2009) and Gomila et al. (2016) for fault-related fractured rocks, considering that 3D fracture surface area accounts for both sides of the fracture-matrix interface, hence, doubling the d_f measurements, when compared with the 2D values calculated by Gomila et al. (2016).
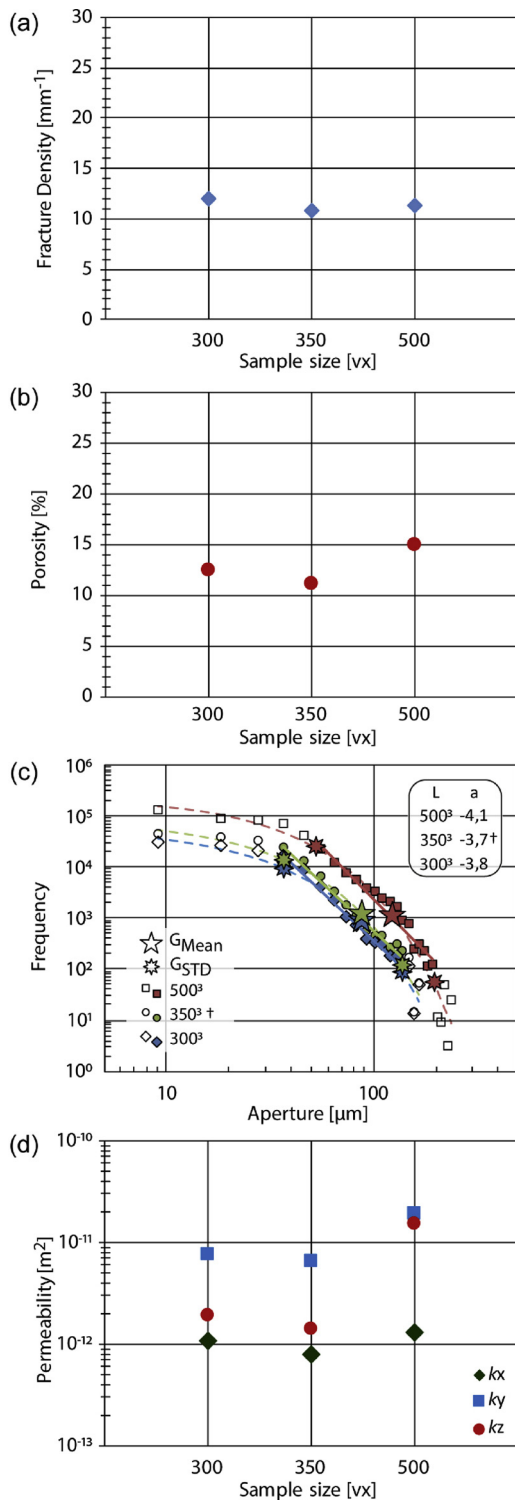
Fig. 10. Comparison of the calculated results with the proposed methodology for the modeled sub-volumes. a) Fracture density and, b) Fracture porosity results for modeled sub-volumes. c) Aperture distributions comparison for the different sub-volumes. Exponential (dashed lines) and power law (solid lines) best fits for the entire and selected data sets (in open and filled symbols), respectively. Geometrical means (G$_{mean}$) and Geometrical standard deviations (G$_{STD}$) for each exponential best fit, together with the exponent a for the power law best fit for each volume size L are also shown. d) Comparison between permeability results for the modeled sub-volumes. (k_z: vertical; k_x: fault perpendicular; k_y: strike parallel).

Fracture aperture distributions in Fig. 8b are best fitted with an exponential distribution. Generally, fracture aperture and fracture length follow a linear relationship in self-similar or fractal fracture networks (Miao et al., 2015; Gong and Rossen, 2017). Hence, exponential distributions of fracture aperture would lead to an exponential distribution of fracture length. A similar relationship has been reported by Zimmermann et al. (2003) for fracture length/aperture distribution in microfractures measured in thin-sections of boreholes of the Continental Deep Drilling Program (KTB). The exponential distribution of fracture length has been associated with early stages of deformation (Cowie et al., 1995; Bonnet et al., 2001), pointing towards the studied sample would represent an early stage in the Jorgillo Fault (regardless of the selected sub-volume). However, another possible explanation for the exponential distribution of fractures apertures relies on the possible truncation and censoring effects (Bonnet et al., 2001; Torabi and Berg, 2011). These sample bias effects are mainly due to the sample size and the resolution of the measurement equipment. Whereas truncation causes underestimation of the frequencies of small fractures (close to the resolution limit), censoring would cause the same effect but for larger fractures (due to the limited size of the sample). If we assume a power law distribution is underlying the exponential distribution (Fig. 10c), it is possible to fix a threshold below and above which the apertures distributions are incompletely mapped. In this work, we used the geometrical standard deviation of the geometrical mean of the fracture apertures as a quantitative method threshold determination (G$_{STD}$ and G$_{Mean}$, respectively; Fig. 10c), and thus use the remaining fracture distribution as a power law. The results of such an approach are in Fig. 10c, where the power law exponents a are 4.1, 3.7 and 3.8 for the different sub-samples of 500^3, 350^3 and 300^3 voxels, respectively. These power law exponents would add an upper boundary to the ones reported by Bonnet et al. (2001; and references therein), considering that power law exponent (a) obtained from 2D analyses, when compared with the ones from 3D analyses, are linked by the relationship $a_{2D} = a_{3D} - 1$. (Davy et al., 2010). This changes in the exponent of the power law exponents may indicate an anisotropy in fracture distribution within the sample.

Permeability simulations were done for the different sample sizes following the same proposed procedure. Modeled values show palaeo-permeability is anisotropic through the sample. The modeled palaeo-permeability values (Fig. 9) are comparable showing similar results throughout the different sub-volume sizes (Fig. 10d). However, pa-laeopermeability is reduced by one order of magnitude in the vertical direction (k_z), when the volume is also reduced. This points toward the idea that relatively big vertical - fault parallel microfractures are responsible for channeling vertical influx of fluids in strike-slip systems, whereas palaeopermeability in the fault-perpendicular direction (k_x) remains almost the same, suggesting small microfractures are controlling the connectivity in such direction.

Despite this reduction in the permeability values, the anisotropy pattern is maintained ($k_x = k(minimum)$, $k_y = k(maximum)$) through all the sub-volumes sizes. This anisotropic behavior of the palaeopermeability, together with the shift of the power law exponent of fracture aperture distribution from 4.1 to 3.7, suggest the positions of the fractures are not randomly distributed within the sub-volumes at the studied scale, and is interpreted as being influenced by the magmatic anisotropy (magmatic layering) of the rock.

4. Concluding remarks

The estimation of the geometrical and hydraulic properties of the fault-related fractured sample is a crucial factor in many areas of the geosciences. Thus the acquisition and quantification of such data are of great importance. This work presents the development of a methodology flow for the proper quantification of this 3D properties, at the microscopic scale, with an easy to follow step-by-step implementation using a combination of µ-CT, open-source software and scripts, and

numerical methods.

Our proposed open-source implementation offers the advantage that once the sample preparation is performed, it is possible to maintain the sample orientation from the physical to the virtual world, hence making possible to assess any possible permeability anisotropies after modeling.

This user-dependent implementation has shown, as a drawback, that the segmentation procedure is the most time-consuming, as in the presence of thin fractures or alteration minerals with the same gray-scale values as the sealed-microfractures, a manual segmentation process must be performed. However, it has also been shown to be fairly easy to learn and fast to use.

By following each step of the methodology, it is possible to constrain both geometrical (i.e., fracture aperture, fracture porosity, fracture specific surface area, and fracture density), and hydraulic (permeability) properties with an emphasis in the proper spatial orientation of a rock sample. Reducing the sub-sample volume by eliminating a major microfracture has shown to be a reliable proxy to determine the flow structure of the selected VOI. Whereas relatively big vertical - fault parallel microfractures are responsible for channeling vertical influx of fluids in this fault-related microfractured rock, palaeopermeability in the fault-perpendicular direction is controlled by the small microfractures within the 3D-volume. The results acquired using the methodology are within range of previously published work, thus proving the reliability of every step.

Acknowledgments

References

Ahrens, J., Geveci, B., Law, C., 2005. ParaView: An End-User Tool for Large Data Visualization, Visualization Handbook. Elsevier.

Andrä, H., Combaret, N., Dvorkin, J., Glatt, E., Han, J., Kabel, M., Keehm, Y., Krzikalla, F., Lee, M., Madonna, C., Marsh, M., Mukerji, T., Saenger, E.H., Sain, R., Saxena, N., Ricker, S., Wiegmann, A., Zhan, X., 2013. Digital rock physics benchmarks-part I: imaging and segmentation. Comput. Geosci. 50, 25–32. https://doi.org/10.1016/j.cageo.2012.09.005.

Anissofira, A., Latief, F.D.E., 2015. Permeability estimation of crack type and granular type of pore space in a geothermal reservoir using lattice boltzmann method and kozeny-carman relation. World Geotherm. Congress 2015, 19–25.

Arancibia, G., Fujita, K., Hoshino, K., Mitchell, T.M., Cembrano, J., Gomila, R., Morata, D., Faulkner, D.R., Rempe, M., 2014. Hydrothermal alteration in an exhumed crustal fault zone: testing geochemical mobility in the Caleta Coloso fault, Atacama fault system, Northern Chile. Tectonophysics 623, 147–168.

Ayachit, U., 2015. The ParaView Guide: A Parallel Visualization Application. Kitware.

Aydin, A., 2000. Fractures, faults, and hydrocarbon entrapment, migration and flow. Mar. Pet. Geol. 17, 797–814. https://doi.org/10.1016/S0264-8172(00)00020-9.

Baker, D.R., Mancini, L., Polacci, M., Higgins, M.D., Gualda, G.A.R., Hill, R.J., Rivers, M.L., 2012. An introduction to the application of X-ray microtomography to the three-dimensional study of igneous rocks. Lithos 148, 262–276. https://doi.org/10.1016/j.lithos.2012.06.008.

Bazaikin, Y., Gurevich, B., Iglauer, S., Khachkova, T., Kolyukhin, D., Lebedev, M., Lisitsa, V., Reshetova, G., 2017. Effect of CT image size and resolution on the accuracy of rock property estimates. J. Geophys. Res. Solid Earth 122, 1–13. https://doi.org/10.1002/2016JB013575.

Bellot, J.P., 2008. Hydrothermal fluids assisted crustal-scale strike-slip on the Argentat fault zone. Tectonophysics 450, 21–33. https://doi.org/10.1016/j.tecto.2007.12.00.

Bense, V.F., Gleeson, T., Loveless, S.E., Bour, O., Scibek, J., 2013. Fault zone hydrogeology. Earth. Rev. 127, 171–192. https://doi.org/10.1016/j.earscirev.2013.09.008.

Berg, C.F., 2014. Permeability description by characteristic length, Tortuosity, constriction and porosity. Transp. Porous Media 103, 381–400. https://doi.org/10.1007/s11242-014-0307-6.

Berkowitz, B., 2002. Characterizing flow and transport in fractured geological media: a review. Adv. Water Resour. 25, 861–884. https://doi.org/10.1016/S0309-1708(02)00042-8.

Boles, J.R., Eichhubl, P., Garven, G., Chen, J., 2004. Evolution of a hydrocarbon migration pathway along basin-bounding faults: evidence from fault cement. Bull. 88, 947–970. https://doi.org/10.1306/02090403040.

Bonnet, E., Bour, O., Odling, N.E., Davy, P., Main, I., Cowie, P., Berkowitz, B., 2001. Scaling of fracture systems in geological media. Rev. Geophys. 39, 347–383. https://doi.org/10.1029/1999RG000074.

Boutareaud, S., Wibberley, C.A.J., Fabbri, O., Shimamoto, T., 2008. Permeability structure and co-seismic thermal pressurization on fault branches: insights from the Usukidani fault, Japan. Geological Society, London, vol. 299. Special Publications, pp. 341–361. https://doi.org/10.1144/SP299.20.

Brogi, A., 2008. Fault zone architecture and permeability features in siliceous sedimentary rocks: insights from the Rapolano geothermal area (Northern Apennines, Italy). J. Struct. Geol. 30, 237–256. https://doi.org/10.1016/j.jsg.2007.10.004.

Brooks, R.A., Di Chiro, G., 1976. Beam hardening in X-ray reconstructive tomography. Phys. Med. Biol. 21, 390–398. https://doi.org/10.1088/0031-9155/21/3/004.

Buades, A., Coll, B., Morel, J.M., 2008. A non-local image and movie denoising. Int. J. Comput. Vis. 76, 123–139. https://doi.org/10.1007/s11263-007-0052-1.

Bultreys, T., De Boever, W., Cnudde, V., 2016. Imaging and image-based fluid transport modeling at the pore scale in geological materials: a practical introduction to the current state-of-the-art. Earth. Rev. 155, 93–128. https://doi.org/10.1016/j.earscirev.2016.02.001.

Caine, J.S., Evans, J.P., Forster, C.B., 1996. Fault zone architecture and permeability structure. Geology 24, 1025–1028. https://doi.org/10.1130/0091-7613(1996)024<1025.

Christensen, M., Tanino, Y., 2017. Enhanced permeability due to apparent oil/brine slippage in limestone and its dependence on wettability. Geophys. Res. Lett. 44, 6116–6123. https://doi.org/10.1002/2017GL073603.

Cnudde, V., Boone, M.N., 2013. High-resolution X-ray computed tomography in geosciences: a review of the current technology and applications. Earth Sci. Rev. 123, 1–17. https://doi.org/10.1016/j.earscirev.2013.04.003.

Cowie, P.A., Sornette, D., Vanneste, C., 1995. Multifractal scaling properties of a growing fault population. Geophys. J. Int. 122, 457–469. https://doi.org/10.1111/j.1365-246X.1995.tb07007.x.

Cox, S.F., Braun, J., Knackstedt, M.A., 2001. Principles of structural control on permeability and fluid flow in hydrothermal systems. Rev. Econ. Geol. 14, 1–24.

Craw, D., Campbell, J.R., 2004. Tectonic and structural setting for active mesothermal gold vein systems, Southern Alps, New Zealand. J. Struct. Geol. 26, 995–1005. https://doi.org/10.1016/j.jsg.2003.11.012.

Davy, P., Bour, O., de Dreuzy, J.R., Darcel, C., 2006. Flow in multiscale fractal fracture networks. Fract. Anal. Nat. Hazards 261, 31–45. https://doi.org/10.1144/GSL.SP.2006.261.01.03.

Davy, P., Le Goc, R., Darcel, C., Bour, O., de Dreuzy, J.R., Munier, R., 2010. A likely universal model of fracture scaling and its consequence for crustal hydromechanics. J. Geophys. Res. 115, 1–13. https://doi.org/10.1029/2009JB007043.

De Boever, W., Derluyn, H., Van Loo, D., Van Hoorebeke, L., Cnudde, V., 2015. Data-fusion of high resolution X-ray CT, SEM and EDS for 3D and pseudo-3D chemical and structural characterization of sandstone. Micron 74, 15–21. https://doi.org/10.1016/j.micron.2015.04.003.

Degruyter, W., Burgisser, A., Bachmann, O., Malaspinas, O., 2010. Synchrotron X-ray microtomography and lattice Boltzmann simulations of gas flow through volcanic pumices. Geosphere 6, 470. https://doi.org/10.1130/GES00555.1.

Deng, H., Fitts, J.P., Peters, C.A., 2016. Quantifying fracture geometry with X-ray tomography: technique of Iterative Local Thresholding (TILT) for 3D image segmentation. Comput. Geosci. 20, 231–244. https://doi.org/10.1007/s10596-016-9560-9.

Dougherty, R., Kunzelmann, K.-H., 2007. Computing local thickness of 3D structures with ImageJ. Microsc. Microanal. 13, 1678–1679. https://doi.org/10.1017/S1431927607074430.

Evans, J.P., Shipton, Z.K., Pachell, M.A., Lim, S.J., Robeson, K., 1999. The structure and composition of exhumed faults, and their implications for seismic processes. Geology 1–15.

Faulkner, D.R., Jackson, C.A.L., Lunn, R.J., Schlische, R.W., Shipton, Z.K., Wibberley, C.A.J., Withjack, M.O., 2010. A review of recent developments concerning the structure, mechanics and fluid flow properties of fault zones. J. Struct. Geol. 32, 1557–1575. https://doi.org/10.1016/j.jsg.2010.06.009.

Faulkner, D.R., Rutter, E.H., 2001. Can the maintenance of overpressured fluids in large strike-slip fault zones explain their apparent weakness? Geology 29, 503–506. https://doi.org/10.1130/0091-7613(2001)029<0503:CTMOOF>2.0.CO;2.

Feldkamp, L.A., Davis, L.C., Kress, J.W., 1984. Practical cone-beam algorithm. J. Opt. Soc. Am. A 1, 612–619. https://doi.org/10.1364/JOSAA.1.000612.

Vision, Fraunhofer-Allianz, 2012. Volume Explorer Software. Volex.

Gomila, R., Arancibia, G., Mitchell, T.M., Cembrano, J.M., Faulkner, D.R., 2016. Palaeopermeability structure within fault-damage zones: a snap-shot from microfracture analyses in a strike-slip system. J. Struct. Geol. 83, 103–120. https://doi.org/10.1016/j.jsg.2015.12.002.

Gong, J., Rossen, W.R., 2017. Modeling flow in naturally fractured reservoirs: effect of fracture aperture distribution on dominant sub-network for flow. Pet. Sci. 14, 138–154. https://doi.org/10.1007/s12182-016-0132-3.

Grader, A.S., Clark, A.B.S., Al-Dayyani, T., Nur, A., 2009. Computations of porosity and permeability of Sparic carbonate using multi-scale CT images. International Symposium of the Society of Core Analysts. pp. 10.

Guibert, R., Nazarova, M., Horgue, P., Hamon, G., Creux, P., Debenest, G., 2015. Computational permeability determination from pore-scale imaging: sample size, mesh and method sensitivities. Transp. Porous Media 107, 641–656. https://doi.org/10.1007/s11242-015-0458-0.

Hirono, T., Lin, W., Yeh, E., Soh, W., Murayama, M., 2009. Porosity profile within the Taiwan Chelungpu Fault, reconstructed from X-ray computed tomography images. JAMSTEC Rep. Res. Dev. 9, 15–22.

Hung, J.H., Ma, K.F., Wang, C.Y., Ito, H., Lin, W., Yeh, E.C., 2009. Subsurface structure, physical properties, fault-zone characteristics and stress state in scientific drill holes of Taiwan Chelungpu fault drilling Project. Tectonophysics 466, 307–321. https://doi.org/10.1016/j.tecto.2007.11.014.

Jarzyna, J.A., Krakowska, P.I., Puskarczyk, E., Wawrzyniak-Guz, K., Bielecki, J., Tkocz, K., Tarasiuk, J., Wroński, S., Dohnalik, M., 2016. X-ray computed micro-tomography—a useful tool for petrophysical properties determination. Comput. Geosci. 20, 1155–1167. https://doi.org/10.1016/s10596-016-9582-3.

Jeanne, P., Guglielmi, Y., Cappa, F., 2013. Hydromechanical heterogeneities of a mature fault zone: impacts on fluid flow. Groundwater 51, 880–892. https://doi.org/10.1111/gwat.12017.

Ju, Y., Zhang, Q., Zheng, J., Chang, C., Xie, H., 2017. Fractal model and lattice boltzmann method for characterization of non-darcy flow in rough fractures. Sci. Rep. 7, 41380. https://doi.org/10.1038/srep41380.

Karcz, I., Dickman, S.R., 1979. Determination of fracture intensity. Tectonophysics 56, T1–T7. https://doi.org/10.1016/0040-1951(79)90079-9.

Karpyn, Z.T., Grader, A.S., Halleck, P.M., 2007. Visualization of fluid occupancy in a rough fracture using micro-tomography. J. Colloid Interface Sci. 307, 181–187. https://doi.org/10.1016/j.jcis.2006.10.082.

Keehm, Y., Mukerji, T., 2004. Permeability And Relative Permeability From Digital Rocks: Issues On Grid Resolution And Representative Elementary Volume. SEG Annual Meeting, Denver, CO, pp. 1654–1657. https://doi.org/10.1190/1.1845147.

Keehm, Y., Mukerji, T., Nur, A., 2004. Permeability prediction from thin sections: 3D reconstruction and lattice-boltzmann flow simulation. Geophys. Res. Lett. 31, 3–6. https://doi.org/10.1029/2003GL018761.

Ketcham, R.A., Carlson, W.D., 2001. Acquisition, optimiziation and interpretation of {X}-ray computed tomography imagery: applications to the geosciences. Comput. Geosci. 27, 381–400.

Kim, Y.S., Sanderson, D.J., 2004. Similarities between strike-slip faults at different scales and a simple age determining method for active faults. Island Arc 13, 128–143. https://doi.org/10.1111/j.1440-1738.2003.00410.x.

Latief, F.D.E., Fauzi, U., Feranie, S., 2014. Digital isolation technique for reconstruction and visualization of cracks in micro- CT images of geothermal reservoir rock. Microsc. Anal. 28, 13–17.

Li, Y., Chen, P., Cochran, E.S., Vidale, J.E., 2007. Seismic velocity variations on the San Andreas fault caused by the 2004 M 6 parkfield earthquake and their implications. Earth Planets Space 59, 21–31. https://doi.org/10.1186/BF03352018.

Lockner, D.A., Tanaka, H., Ito, H., Ikeda, R., Omura, K., Naka, H., 2009. Geometry of the Nojima fault at Nojima-Hirabayashi, Japan - I. A simple damage structure inferred from borehole core permeability. Pure Appl. Geophys. 166, 1649–1667. https://doi.org/10.1007/s00024-009-0515-0.

Miao, T., Yu, B., Duan, Y., Fang, Q., 2015. A fractal analysis of permeability for fractured rocks. Int. J. Heat Mass Transf. 81, 75–80. https://doi.org/10.1016/j.ijheatmasstransfer.2014.10.010.

Mitchell, T.M., Faulkner, D.R., 2009. The nature and origin of off-fault damage surrounding strike-slip fault zones with a wide range of displacements: a field study from the Atacama fault system, northern Chile. J. Struct. Geol. 31, 802–816. https://doi.org/10.1016/j.jsg.2009.05.002.

Mittempergher, S., Pennacchioni, G., Di Toro, G., 2009. The effects of fault orientation and fluid infiltration on fault rock assemblages at seismogenic depths. J. Struct. Geol. 31, 1511–1524. https://doi.org/10.1016/j.jsg.2009.09.003.

Mizoguchi, K., Hirose, T., Shimamoto, T., Fukuyama, E., 2008. Internal structure and permeability of the Nojima fault, southwest Japan. J. Struct. Geol. 30, 513–524. https://doi.org/10.1016/j.jsg.2007.12.002.

Morrow, C.a., Lockner, D.a., 1994. Permeability differences between surface-derived and deep drillhole core samples. Geophys. Res. Lett. 21, 2151. https://doi.org/10.1029/94GL01936.

Morton, N., Girty, G.H., Rockwell, T.K., 2012. Fault zone architecture of the San Jacinto fault zone in Horse Canyon, southern California: a model for focused post-seismic fluid flow and heat transfer in the shallow crust. Earth Planet. Sci. Lett. 329-330, 71–83. https://doi.org/10.1016/j.epsl.2012.02.013.

Mostaghimi, P., Blunt, M.J., Bijeljic, B., 2013. Computations of absolute permeability on Micro-CT images. Math. Geosci. 45, 103–125. https://doi.org/10.1007/s11004-012-9431-4.

Mutina, A., Koroteev, D., 2012. Using X-ray microtomography for the three dimensional mapping of minerals. Microsc. Anal. 26, 1–4.

Okabe, H., Blunt, M.J., 2004. Prediction of permeability for porous media reconstructed using multiple-point statistics. Phys. Rev. E – Stat. Nonlinear Soft Matter Phys. 70, 1–2. https://doi.org/10.1103/PhysRevE.70.066135.

Perumal, D.A., Dass, A.K., 2015. A Review on the development of lattice Boltzmann computation of macro fluid flows and heat transfer. Alexandria Eng. J. 54, 955–971. https://doi.org/10.1016/j.aej.2015.07.015.

Ran, G., Eyal, S., Yoseph, Y., Amir, S., Noam, W., 2014. The permeability of fault zones: a case study of the Dead Sea rift (Middle East). Hydrogeol. J. 22, 425–440. https://doi.org/10.1007/s10040-013-1055-3.

Roques, C., Bour, O., Aquilina, L., Dewandel, B., Leray, S., Schroetter, J.M., Longuevergne, L., Le Borgne, T., Hochreutener, R., Labasque, T., Lavanent, N., Vergnaud-Ayraud, V., Mougin, B., 2014. Hydrological behavior of a deep sub-vertical fault in crystalline basement and relationships with surrounding reservoirs. J. Hydrol. (Amst) 509, 42–54. https://doi.org/10.1016/j.jhydrol.2013.11.023.

Rowland, J.V., Sibson, R.H., 2004. Structural controls on hydrothermal flow in a segmented rift system, Taupo Volcanic Zone, New Zealand. Geofluids 4, 259–283. https://doi.org/10.1111/j.1468-8123.2004.00091.x.

Schneider, C.A., Rasband, W.S., Eliceiri, K.W., 2012. NIH Image to ImageJ: 25 years of image analysis. Nat. Methods 9, 671–675. https://doi.org/10.1038/nmeth.2089.

Sibson, R.H., 1996. Structural permeability of fluid-driven fault-fracture meshes. J. Struct. Geol. 18, 1031–1042. https://doi.org/10.1016/0191-8141(96)00032-6.

Singhal, B.B.S., Gupta, R.P., 2010. Applied Hydrogeology of Fractured Rocks, second ed. Springer, Netherlands. https://doi.org/10.1007/978-90-481-8799-7.

Sukop, M.C., Thorne, D.T., 2006. Lattice Boltzmann Modeling, An Introduction for Geoscientists and Engineers. Springer-Verlag, Berlin Heidelberg. https://doi.org/10.1007/978-3-540-27982-2.

Sun, W., Andrade, J.E., Rudnicki, J.W., Eichhubl, P., 2011. Connecting microstructural attributes and permeability from 3D tomographic images of in situ shear-enhanced compaction bands using multiscale computations. Geophys. Res. Lett. 38, 1–5. https://doi.org/10.1029/2011GL047683.

Tarquis, A.M., Heck, R.J., Grau, J.B., Fabregat, J., Sanchez, M.E., Antón, J.M., 2008. Influence of thresholding in mass and entropy dimension of 3-D soil images. Nonlinear Process. Geophys. 15, 881–891. https://doi.org/10.5194/npg-15-881-2008.

Torabi, A., Berg, S.S., 2011. Scaling of fault attributes: a review. Mar. Pet. Geol. 28, 1444–1460. https://doi.org/10.1016/j.marpetgeo.2011.04.003.

Tripp, G.I., Vearncombe, J.R., 2004. Fault/fracture density and mineralization: a contouring method for targeting in gold exploration. J. Struct. Geol. 26, 1087–1108. https://doi.org/10.1016/j.jsg.2003.11.002.

Uehara, S., Shimamoto, T., 2007. Permeability of fault rocks from the median tectonic in Ohshika-mura, Nagano, Japan as studied by pressure-cycling tests. Geological Society 289. London, Special Publications, pp. 143–160. https://doi.org/10.1144/SP289.9.

Vlahinić, I., Andò, E., Viggiani, G., Andrade, J.E., 2014. Towards a more accurate characterization of granular media: extracting quantitative descriptors from tomographic images. Granul. Matter 16, 9–21. https://doi.org/10.1007/s10035-013-0460-6.

Voorn, M., Exner, U., Barnhoorn, A., Baud, P., Reuschlé, T., 2015. Porosity, permeability and 3D fracture network characterisation of dolomite reservoir rock samples. J. Pet. Sci. Eng. 127, 270–285. https://doi.org/10.1016/j.petrol.2014.12.019.

Voorn, M., Exner, U., Rath, A., 2013. Multiscale Hessian fracture filtering for the enhancement and segmentation of narrow fractures in 3D image data. Comput. Geosci. 57, 44–53. https://doi.org/10.1016/j.cageo.2013.03.006.

Walsh, J.B., Brace, W.F., 1984. The effect of pressure on porosity and the transport properties of rock. J. Geopys. Res. 89, 9425–9431. https://doi.org/10.1016/0148-9062(85)93020-7.

Watanabe, N., Egawa, M., Sakaguchi, K., Ishibashi, T., Tsuchiya, N., 2017. Hydraulic fracturing and permeability enhancement in granite from subcritical/brittle to supercritical/ductile conditions. Geophys. Res. Lett. 44, 5468–5475. https://doi.org/10.1002/2017GL073898.

Wibberley, C.A.J., Shimamoto, T., 2003. Internal structure and permeability of major strike-slip fault zones: the median tectonic line in Mie Prefecture, Southwest Japan. J. Struct. Geol. 25, 59–78. https://doi.org/10.1016/S0191-8141(02)00014-7.

Wildenschild, D., Sheppard, A.P., 2013. X-ray imaging and analysis techniques for quantifying pore-scale structure and processes in subsurface porous medium systems. Adv. Water Resour. 51, 217–246. https://doi.org/10.1016/j.advwatres.2012.07.018.

Yushkevich, P.A., Piven, J., Hazlett, H.C., Smith, R.G., Ho, S., Gee, J.C., Gerig, G., 2006. User-guided 3D active contour segmentation of anatomical structures: significantly improved efficiency and reliability. NeuroImage 31, 1116–1128. https://doi.org/10.1016/j.neuroimage.2006.01.015.

Zhang, Y., Schaubs, P.M., Sheldon, H.A., Poulet, T., Karrech, A., 2013. Modelling fault reactivation and fluid flow around a fault restraining step-over structure in the Laverton gold region, Yilgarn Craton, Western Australia. Geofluids 13, 127–139. https://doi.org/10.1111/gfl.12012.

Zimmermann, G., Burkhardt, H., Engelhard, L., 2003. Scale dependence of hydraulic and structural parameters in fractured rock, from borehole data (KTB and HSDP). Geological Society, vol. 240. Special Publications, London, pp. 37–45. https://doi.org/10.1144/GSL.SP.2005.240.01.04.